

# Anomalous radio emission from dust in the Helix

S. Casassus<sup>1</sup>, A.C.S. Readhead<sup>2</sup>, T.J. Pearson<sup>2</sup>, L.-Å. Nyman<sup>3</sup>,  
M.C. Shepherd<sup>2</sup>, L. Bronfman<sup>1</sup>

## ABSTRACT

A byproduct of experiments designed to map the cosmic microwave background is the recent detection of a new component of foreground Galactic emission. The anomalous foreground at  $\sim 10\text{--}30$  GHz, unexplained by traditional emission mechanisms, correlates with  $100\mu\text{m}$  dust emission. We use planetary nebulae (PNe) as astrophysical laboratories to test known radio emission processes, and report that in the Helix the emission at 31 GHz and  $100\mu\text{m}$  are well correlated, and exhibit similar features on sky images, which are absent in  $H\beta$ . Upper limits on the 250 GHz continuum emission in the Helix rule out cold grains as candidates for the 31 GHz emission, and provide spectroscopic evidence for an excess at 31 GHz over bremsstrahlung. We estimate that the  $100\mu\text{m}$ -correlated radio emission, presumably due to dust, accounts for at least 20% of the 31 GHz emission in the Helix. This result strengthens previous tentative interpretations of diffuse interstellar medium spectra involving a new dust emission mechanism at radio frequencies. Very small grains, thought not to survive in evolved PNe, have not been detected in the Helix, which hampers interpreting the new component in terms of electric dipole emission from spinning grains. The observed iron depletion in the Helix favors considering the identity of this new component to be magnetic dipole emission from hot ferromagnetic grains. The reduced level of free-free continuum we report also implies an electronic temperature of  $T_e = 4600 \pm 1200$  K for the free-free emitting material, which is significantly lower than the temperature of  $9500 \pm 500$  K inferred from collisionally-excited lines.

*Subject headings:* planetary nebulae: individual (NGC 7293), radio continuum: ISM, radiation mechanisms: general, infrared: ISM, ISM: dust, Cosmology: Cosmic Microwave Background

---

<sup>1</sup>Departamento de Astronomía, Universidad de Chile, Santiago, Casilla 36-D, Chile

<sup>2</sup>Owens Valley Radio Observatory, California Institute of Technology, Pasadena, CA 91125

<sup>3</sup>Onsala Space Observatory, 439 92 Onsala, Sweden

## 1. Introduction

Continuum emission mechanisms from ionized nebulae or from the diffuse interstellar medium (ISM) at radio frequencies (lower than  $\sim 90$  GHz), have up to now been attributed to two components: Free-free emission (thermal bremsstrahlung), or synchrotron emission. But the problem of separating Galactic foregrounds from cosmic microwave background (CMB) radiation has motivated a careful review of the emission mechanisms from the ISM. Dust-correlated radio emission, with hints of anomalous spectral properties, has first been reported in the analysis of *COBE* data (Kogut et al. 1996). The ‘anomalous foreground’ detected at 14 GHz by Leitch et al. (1997) correlates with *IRAS* 100 $\mu$ m maps, and has a flat spectral index characteristic of free-free emission, but the corresponding H $\alpha$  emission is absent. Draine & Lazarian (1998) rule out, on energetic grounds, hot plasma interpretations of the anomalous foreground, and propose a model in which it is due to electric dipole radiation from spinning very small dust grains (VSGs). Their proposition has found verification from statistical evidence brought forward by de Oliveira-Costa et al. (1999, 2002).

Finkbeiner et al. (2002) have detected a spectral energy distribution (SED) that is inconsistent with free-free emission for the 100  $\mu$ m-correlated radio emission in the diffuse H II region LPH 201.663+1.643 (LPH 201.6 hereafter). But the interpretation of the SED of LPH 201.6 in terms of the Draine & Lazarian (1998) models meets two difficulties. One is the premise that radio emission in LPH 201.6 is proportional to far-IR dust emission. Another difficulty is that the positive 5-10 GHz spectral index reported by Finkbeiner et al. could also be accounted for by unresolved optically thick emission (McCullough & Chen 2002).

It would seem that apart from well-studied free-free and synchrotron emission, there is an additional component in the SED of the diffuse ISM. Are there ways to constrain the many free parameters in the Draine & Lazarian (1998) model, such as the precise identity of the spinning VSGs? Is spinning dust ubiquitous in the Galaxy? Is it important in objects such as planetary nebulae (PNe), or H II regions? What is the importance of magnetic dipole emission from classical grains, also proposed by Draine & Lazarian (1999)? Improved knowledge of these new emission mechanisms is crucial to the interpretation of radio-continuum observations as a diagnostic of physical conditions.

Planetary nebulae are perhaps the simplest of ionized nebulae: an ionized expanding envelope around an exposed stellar core. Their being bright and isolated objects and their relative simplicity compared to star-forming regions has given PNe a central role in the development of nebular astrophysics (e.g. Osterbrock 1989). Evolved PNe, and in particular NGC 7293 (the Helix), are important for the study of the late stages of PN evolution and feed-back into the ISM. The large angular size of the Helix, about 10 arcmin in diameter,

stems from its proximity, at a distance of  $\sim 200$  pc (Harris et al. 1997), but also from its huge physical size compared to other PNe, with emission traced at diameters of up to 1 pc (Speck et al. 2002). The large sizes and ages of evolved PNe make them useful probes of nebular structure, and of dust grain survival in the PN phase. But it is their very size which makes their observation difficult, especially at radio frequencies.

Resolved radio-frequency images of the Helix are scarce. Zijlstra et al. (1989), as part of an imaging survey of PNe with the VLA, reported a 14.9 GHz map of the Helix. The NRAO VLA Sky Survey (Condon et al. 1998, NVSS) detected the brightest clumps of the nebular ring, but a more sensitive 1.4 GHz image was obtained by Rodriguez et al. (2002). These three images are heavily affected by flux losses: because of incomplete sampling in the  $uv$  plane the reconstructed images have missing spatial frequencies, and part of the extended nebular emission is lost. The 1.4 GHz high resolution images reveal the presence of bright background sources within the nebular diameter, which distort low resolution images and spoil integrated nebular flux density measurements at low frequencies.

Here we report evidence that 31 GHz emission in the Helix is due not only to free-free emission, as currently thought, but also to a new dust grain emission mechanism, other than the traditional thermal emission from vibrations of the charge distribution (Draine & Lazarian 1999). Part of the 31 GHz emission shares similar characteristics with the anomalous CMB foreground due to the diffuse ISM. The discovery of a new radio dust emission mechanism is the first in a specific object as well studied as the Helix, and strengthens the tentative interpretation of the SED of LPH 201.6 proposed by Finkbeiner et al. (2002).

We have used the Cosmic Background Imager (CBI) to map the Helix at 31 GHz, which allows us to present integrated flux densities and spatially resolved images at low resolution, but with little flux loss. We find the background sources visible in the 1.4 GHz images of the Helix are negligible at 31 GHz. In addition we have used the Sest IMaging Bolometer Array (Nyman et al. 2001, SIMBA), at the Swedish-ESO Submillimetre Telescope (SEST) to search for possible cold dust emission at 250 GHz, and to obtain a comparison flux density for the 31 GHz data, to explore the SED of evolved PNe. The Helix is not detected in the SIMBA image, but the observations allow us to put upper limits on the nebular flux at 250 GHz. The SIMBA observations are complemented by weaker upper limits from the *WMAP* first-year data release (Bennett et al. 2003).

The CBI observations of the Helix, which constitute the first maps of the anomalous dust-correlated emission, are presented in Section 2, along with a discussion of flux losses and background source contamination. The SIMBA upper limits on the radio continuum at 250 GHz are given in Sec. 3. Our results are discussed in the context of the SED of the Helix in Sec. 4, in which we estimate the ionized mass of the Helix to be  $0.096 M_{\odot}$ , with a 30%

accuracy. Sec. 5 concludes. We use the Perl Data Language (<http://pdl.perl.org>) for all data analysis, unless otherwise stated.

## 2. CBI observations

The CBI (Padin et al. 2002) is a planar interferometer array with 13 antennas, each 0.9 m in diameter, mounted on a 6 m tracking platform, which rotates in parallactic angle to provide uniform  $uv$ -coverage. It is located in Chajnantor, Atacama, Chile. The CBI receivers operate in 10 frequency channels, with 1 GHz bandwidth each, giving a total bandwidth of 26–36 GHz.

We have observed the Helix (J2000 RA=22:29:38, DEC= -20:50:13) in two different array configurations, resulting in different full-widths at half maximum (FWHM) for the Gaussian fits to the synthesized beam: we have integrated for 4800s on 2001-Sep-7 and Nov-8, with an elliptical beam of  $4.90 \times 4.52$  arcmin<sup>2</sup>, and for 8250s on 2002-Nov-17,18,21,22, with a beam of  $10.1 \times 8.19$  arcmin<sup>2</sup>. Ground emission (spill-over), or the Moon, can enter in the side-lobes of the receivers, and a comparison field, observed at the same elevation as the target, is required for ground or Moon cancellation. This reference field is offset by 8 arcmin in RA, trailing the target, and is observed for the same integration time as the object field.

Flux calibration is performed using Tau A and Saturn, and is described in detail by Mason et al. (2003). The internal calibration consistency on the CBI is better than 1%, and the flux density scale, originally set by absolute calibrations at the Owens Valley Radio Observatory with an uncertainty of 3.3% (Mason et al. 2003), has now been improved by comparison with the WMAP temperature measurement of Jupiter (Page et al. 2003) to an uncertainty of 1.3% (Readhead & Pearson 2003), which is used in this work.

### 2.1. Observed 31 GHz flux densities

To extract the nebular flux density in a photometric aperture, we reconstruct a clean image of the Helix by fitting an image-plane model to the observed visibilities. The clean image is restored by adding the residual dirty map to the model, convolved with the best-fit elliptical beam. Using the ‘modelfit’ task of the difmap package (Shepherd 1997), we find a two component model gives a very good fit to the data: a large elliptical Gaussian roughly following the optical nebular ring, with a negative point source inset in the larger component to account for the central plateau obvious in visible images of NGC 7293 (O’Dell 1998, for instance). For the purpose of extracting an integrated nebular flux density, we prefer the

use of natural weights, which give the lowest noise in the restored image.

The flux density in a circular photometric aperture encompassing the whole nebula is  $992 \pm 35$  mJy in the 2001 data. The aperture radius is set at 15 arcmin, the value beyond which the flux increment is less than its rms uncertainty. For comparison, the flux density in a 12 arcmin aperture is  $934 \pm 28$  mJy. We use the 2002 data for a counter check, and obtain  $1000 \pm 31$  mJy in an optimal aperture of 17 arcmin, or  $966 \pm 26$  mJy in 15 arcmin. Thus our best value for the integrated 31 GHz flux density is  $996 \pm 21$ , obtained by averaging the 2001 and 2002 data (note this is without flux-loss correction, see below).

We estimate the measurement uncertainty by multiplying the noise level in Jy/pixel by  $\sqrt{N N_{\text{beam}}}$ , where  $N$  is the number of pixels within the aperture, and  $N_{\text{beam}}$  is taken to represent the number of correlated pixels (those that fall in one beam). The 10 channel information over 26–36 GHz only places weak constraints on the spectral index: a fit in the form  $\kappa(\nu/31.5)^\alpha$ , where  $\nu$  is the channel frequency in GHz, gives a best fit  $\kappa = 1.01 \pm 0.11$  Jy and  $\alpha = 0.17^{+1.19}_{-1.08}$ , at 68.3% confidence (i.e.  $\sim \pm 1\sigma$ ).

## 2.2. Background source contamination at 31 GHz

Background sources show up distinctively at 1.4 GHz, in Fig. 1 of Rodriguez et al. (2002), and are a problem when reporting integrated fluxes for the Helix. But we do not detect them in our 31 GHz images, presumably because they have sufficiently negative spectral indexes.

To compare with the 1.4 GHz image of the Helix provided by L.F. Rodriguez, we extract the best resolution possible from our 31 GHz visibility data by using the MEM algorithm in AIPS++, restricting to visibilities with  $uv$ -radii greater than 300. An overlay of this image-plane MEM model with the 1.4 GHz image of the Helix, shown in Fig. 1, demonstrates that none of the 1.4 GHz point sources is present at 31 GHz, at least at a level comparable to the nebular specific intensities.

The brightest point source at 1.4 GHz is J2229-2054, with  $\sim 0.1$  Jy in the NVSS image, and 0.15 Jy in Rodriguez et al. (2002), and is 12 times brighter than the next brightest point source within the nebular diameter. As another test on the intensity of the 1.4 GHz point sources in the CBI image, we add to the parametrized image-plane model of the observed visibilities a single point source component, with position fixed at that of J2229-2054, but with a variable flux density. The best-fit model to the CBI visibilities, obtained with ‘modelfit’, gives a flux density of 12 mJy. Thus J2229-2054, if present at 31 GHz, is barely above the noise of the CBI image of 9 mJy/beam.

The black dot on the CBI image in Fig.2 lies at the location of J2229-2054, and is drawn to highlight its absence.

### 2.3. CBI 31 GHz image and comparison with H $\alpha$ , H $\beta$ , 60 $\mu$ m 100 $\mu$ m and 180 $\mu$ m images.

To guide the interpretation of the 31 GHz data, we compare with simulations of the CBI observations on H $\alpha$ , H $\beta$ , 60 $\mu$ m and 100 $\mu$ m template images. We use as input images the continuum-subtracted (CC) Southern H-Alpha Sky Survey Atlas (Gaustad et al. 2001, SHASSA), the H $\beta$  image<sup>4</sup> by O’Dell (1998), the HIRES-reprocessed *IRAS* 60  $\mu$ m and 100  $\mu$ m images<sup>5</sup>, and the *ISO*<sup>6</sup> 180  $\mu$ m image of the Helix obtained with the ISOPHOT camera (Lemke et al. 1996).

Simulation of the CBI observations is performed with the MockCBI program (Pearson 2000, private communication), which calculates the visibilities  $V(u, v)$  on the input images  $I_\nu(x, y)$  with the same  $uv$  sampling as a reference visibility dataset:

$$V(u, v) = \int_{-\infty}^{\infty} A_\nu(x, y) I_\nu(x, y) \exp [2\pi i (ux + vy)] \frac{dx dy}{\sqrt{1 - x^2 - y^2}}, \quad (1)$$

where  $A_\nu(x, y)$  is the CBI primary beam and  $x$  and  $y$  are the direction cosines relative to the phase center in two orthogonal directions on the sky. Thus MockCBI creates the visibility dataset that would have been obtained had the sky emission followed the template. In the case of the H $\beta$  input image, care is taken to remove bright stars. The template images have much finer resolution than the CBI synthesized beam, so that their final resolution is essentially the same as that of the CBI images.

The restored images are shown in Fig. 2. We use the fitting of model components, as explained in Sec.2.1, but this time restoring with uniform weights, with an additional radial weight to improve resolution. The 31 GHz data faithfully reflects none of the comparison images. Rather, it seems to correspond to a combination of all, with a stronger resemblance

---

<sup>4</sup>obtained from Romano Corradi’s web page [www.ing.iac.es/~rcorradi/HALOES/](http://www.ing.iac.es/~rcorradi/HALOES/)

<sup>5</sup>with default options, see [irsa.ipac.caltech.edu/IRASdocs/hires\\_proc.html](http://irsa.ipac.caltech.edu/IRASdocs/hires_proc.html)

<sup>6</sup>ISO is an ESA project with instruments funded by ESA Member States (especially the PI countries: France, Germany, the Netherlands and the United Kingdom) and with the participation of ISAS and NASA. The ISO TDT and AOT codes for the image used here are 16701206 and PHT22, and the observer is P. Cox. Note the calibrated 180  $\mu$ m image is affected by a constant offset, by about the same amount as the peak nebular intensity, which probably reflects calibration problems.

to the 180  $\mu\text{m}$  and 100  $\mu\text{m}$  image than to the 60 $\mu\text{m}$  and  $\text{H}\beta$  images. The 31 GHz emission is localized in two bright North and South clumps (N-S clumps), each with East and West extensions (E-W lobes). The N-S clumps at 31 GHz reflect the  $\text{H}\beta$  image, and are slightly offset from their far-IR counterparts. But the E-W lobes are absent in  $\text{H}\beta$ . The differences between  $\text{H}\beta$  and 31 GHz are best appreciated in the lower-right panel of Fig. 2, where we have subtracted from the 31 GHz image the  $\text{H}\beta$  template scaled to the expected level of free-free emission (see below). The remainder of this subtraction is the anomalous emission: It cannot be accounted for by free-free emission.

It can be noted that the anomalous emission map and the *ISO* 180  $\mu\text{m}$  maps share similar morphologies, although the later is more extended. The 100  $\mu\text{m}$  and 60  $\mu\text{m}$  are also more compact than the 180  $\mu\text{m}$  map, as expected from grain heating due to central star radiation, but the E-W lobes do not show as markedly as in the 180  $\mu\text{m}$  map. The anomalous emission isn't as sharply confined to the N-S clumps, and has a very bright Western lobe relative to the rest of the nebula. The only other map with such a bright Western lobe is the ISOCAM 5–8.5  $\mu\text{m}$  map from Cox et al. (1999, they refer to the Western lobe as the Western rim), which is dominated by  $\text{H}_2$  line emission (see Fig. 3).

The  $\text{H}\alpha$  simulated images with the SHASSA templates have essentially the same morphology as the  $\text{H}\beta$  simulation, which serves as cross check. We prefer the  $\text{H}\beta$  data since  $[\text{N II}]$ , which arises mostly in the nebular ring, contaminates the SHASSA narrow band filter up to 50% of the total flux. The  $[\text{N II}]$  contamination is reflected in the  $\text{H}\alpha$  flux from the SHASSA image, which is twice the value from O'Dell (1998) (scaled for the Balmer decrement): Transmission for the two  $[\text{N II}]$  lines is about 50% while their flux is about twice the  $\text{H}\alpha$  flux.

To illustrate that the morphological trends shown in Fig. 2 are not artifacts of the deconvolutions, we present in Fig. 3 a comparison of the ISOPHOT 180  $\mu\text{m}$ , the HIRES 100  $\mu\text{m}$  images, the ISOCAM LW2 map<sup>7</sup>, and the SHASSA CC image. The SHASSA image is better suited than the  $\text{H}\beta$  image for comparison with the far-IR data because it is closer in resolution, and because most stars are removed in the continuum subtraction. The morphological differences between dust and  $\text{H}\alpha$  are apparent, while the 180  $\mu\text{m}$ -100  $\mu\text{m}$  similarity renders improbable their contamination from emission lines.

---

<sup>7</sup>ISO TDT 16701502

## 2.4. Flux loss estimates

The Helix is extended and resolved by the CBI, and there is bound to be a measure of flux loss derived from missing low spatial frequencies in the CBI’s  $uv$  coverage. We now estimate the amount of flux loss with the template images mentioned in Sec. 2.3. We simulate the 2001 CBI observations using MockCBI, and after reconstructing with natural weights, in the same manner as described in Sec. 2.1 for the CBI data, we extract the integrated nebular flux density and compare with the input map. This strategy also allows estimating systematic errors on the integrated flux derived from the image reconstruction.

In the case of the  $100\mu\text{m}$  image, the flux density in a circular aperture of 15 arcmin in radius, as for the CBI photometry, dropped from 305.8 Jy to 272.3 Jy, which means 89.0% of the flux density was recovered. We repeated the same exercise on the continuum-corrected SHASSA image, recovering 92.0% of the flux, and 90.0% in the case of the  $\text{H}\beta$  image. The finest resolution is that of the  $\text{H}\beta$  image, which probably best reflects the flux lost.

Therefore we estimate that 90% of the flux is recovered by the CBI in the  $15'$  circular photometric aperture we are using, and the actual flux density of the Helix at 31 GHz is 1096 mJy, with a  $\sim 10\%$  uncertainty.

## 2.5. Cross-correlations between CBI and template visibilities

Here we cross-correlate the CBI data with the comparison templates, in order to quantify the resemblance of the 31 GHz image to the *IRAS* data. The  $100\mu\text{m}$  correlation is particularly interesting because it is a comparison point with previous work on the anomalous foreground.

We investigate a model in which the 31 GHz specific intensities,  $\vec{y}$ , result from a linear combination of various components, as in de Oliveira-Costa et al. (2002) and Finkbeiner et al. (2002):  $\vec{y} = \sum_{i=1}^N a_i^N \vec{x}_i$ , where  $N$  is the number of templates  $\vec{x}_i$ . We fit for conversion factors, with  $N = 1$ ,  $\vec{y} = a_{100\mu\text{m}}^I \vec{x}_{100\mu\text{m}}$  and  $\vec{y} = a_{\text{H}\beta}^I \vec{x}_{\text{H}\beta}$ , and for a linear combination of the  $\text{H}\beta$  and  $100\mu\text{m}$  templates,  $N = 2$ ,  $\vec{y} = a_{\text{H}\beta}^{II} \vec{x}_{\text{H}\beta} + a_{100\mu\text{m}}^{II} \vec{x}_{100\mu\text{m}}$ . We also try fitting for a general cross-correlation, with all templates,  $N = 4$ :  $\vec{y} = \sum_i a_i^{IV} \vec{x}_i = a_{\text{H}\beta}^{IV} \vec{x}_{\text{H}\beta} + a_{100\mu\text{m}}^{IV} \vec{x}_{100\mu\text{m}} + a_{60\mu\text{m}}^{IV} \vec{x}_{60\mu\text{m}} + a_{180\mu\text{m}}^{IV} \vec{x}_{180\mu\text{m}}$ . In our notation the roman number superscripts on the linear coefficients refer to  $N$ , the number of templates used in the fits.

Because of the linearity of the Fourier transform, the same relationships hold for the complex visibilities and specific intensities, provided the relationships are realistic. We performed the cross-correlations both on the sky images and in frequency space, shown in Fig. 4,

confirming the results within the uncertainties, which adds confidence in the linear combinations. Proportionality between 31 GHz and the templates might not hold, for instance, in the case of free-free emission, which is proportional to the emission measure, and far-IR dust emission, which is proportional to the column of dust. One justification for a 31 GHz–100  $\mu\text{m}$  conversion factor might be that the diffuse UV nebular field makes an important contribution to grain heating, another that dust emission is important at 31 GHz.

The cross-correlation results are shown in Table 1. It can be appreciated from the two component fit ( $a_{\text{H}\beta}^{II}$  and  $a_{100\mu\text{m}}^{II}$ ) that part of the 31 GHz visibilities correlate with the 100  $\mu\text{m}$  visibilities, and part with H $\beta$ . No significant correlation exists with 60  $\mu\text{m}$  and 180  $\mu\text{m}$ . We found no trends with baseline length within the uncertainties.

The significance of the linear combination fits are difficult to assess because the template images are smoothed versions of the original maps, and their noise is undetermined. But we can use as guideline the reduced  $\chi^2$  in the absence of noise in the templates, which are  $\chi_{II}^2(100\mu\text{m}) = 1.0971$ ,  $\chi_{II}^2(\text{H}\beta) = 1.0836$ ,  $\chi_{II}^2 = 1.0829$  and  $\chi_{IV}^2 = 1.0821$ . If the noise level in the templates is at  $10^{-3}$  the rms visibility values, then  $\chi_{II}^2(\text{H}\beta) = 1.0836$ ,  $\chi_{II}^2(100\mu\text{m}) = 1.0609$ ,  $\chi_{II}^2 = 1.0280$  and  $\chi_{IV}^2 = 0.9897$ . Thus the best fit model seems to be model *IV*, then model *II*, followed by model *I* with the 100  $\mu\text{m}$  template if noise is included.

Our 100 $\mu\text{m}$ –31 GHz conversion factor  $a_{100\mu\text{m}}^I = 3.61(7) 10^{-3}$  is close in value to that reported by Finkbeiner et al. (2002) for the conversion from 100 $\mu\text{m}$  to 10 GHz. After scaling units (our  $a_{100\mu\text{m}}^I$  is dimensionless), the value for LPH 201.6 from Finkbeiner et al. (2002) is  $3.84 10^{-3}$  at 10 GHz. However, we caution that Finkbeiner et al. (2002) compared with the 100  $\mu\text{m}$  map from Schlegel et al. (1998), which cannot be used for the Helix because of insufficient angular resolution. The Schlegel et al. (1998) 100  $\mu\text{m}$  flux density is  $\sim 30\%$  higher than the HIRES-reprocessed IRAS flux density, both for the Helix and LPH 201.6. Had we used an integrated flux density conversion factor and the Schlegel et al. (1998) 100  $\mu\text{m}$  flux density, our value for  $a_{100\mu\text{m}}^I$  would have been 30% lower.

On the other hand our value for  $a_{100\mu\text{m}}^I$  differs from that reported by de Oliveira-Costa et al. (2002) for Galactic latitudes  $|b| > 20^\circ$ , which is  $2.2 10^{-4}$  at 10 GHz and  $3.6 10^{-4}$  at 15 GHz. In de Oliveira-Costa et al. (2002) the 15 GHz diffuse Galactic emission is modeled by a three component linear fit, with H $\alpha$ , 100  $\mu\text{m}$  and synchrotron templates. The synchrotron component decreases significantly from 10 GHz to 15 GHz, so if it is negligible at 15 GHz, their 100  $\mu\text{m}$  coefficient could perhaps be compared to our value for  $a_{100\mu\text{m}}^{II} = 0.75(40) 10^{-3}$ , which agrees within the uncertainties.

It must be noted that the conversion factors from de Oliveira-Costa et al. (2002), Finkbeiner et al. (2002), and our work are not strictly comparable because they correspond

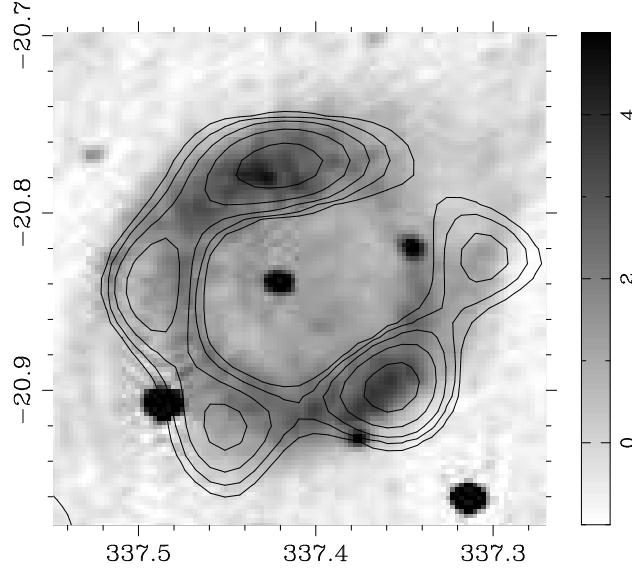


Fig. 1.— The MEM model of the 31 GHz CBI visibilities of the Helix in contours, overlaid on a grey scale image at 1.4 GHz of the same region (Rodriguez et al. 2002). All contour levels are increasing. The  $x$ -axis and  $y$ -axis are J2000 right ascension (RA), and declination (DEC), both in degrees.

Table 1. Cross-correlation results, given in the format  $a_i \pm \sigma(a_i) [a_i/\sigma(a_i)]$ .  $H\beta$  entries have units of  $10^{12}$  Jy /  $W m^{-2}$ , and all others have dimensionless units of  $10^{-3}$ . The cross-correlations have been performed on the real part of the visibilities, for the full  $uv$ -range of  $88.4 - 622 \text{ rad}^{-1}$ . Note we convert between flux densities, not brightness temperatures.

$a_{H\beta}^I$	$a_{100\mu\text{m}}^I$	$a_{H\beta}^{II}$	$a_{100\mu\text{m}}^{II}$
$2.65 \pm 0.05[55]$	$3.61 \pm 0.07[55]$	$2.12 \pm 0.29[7.2]$	$0.75 \pm 0.40[1.9]$
$a_{H\beta}^{IV}$	$a_{100\mu\text{m}}^{IV}$	$a_{60\mu\text{m}}^{IV}$	$a_{180\mu\text{m}}^{IV}$
$3.05 \pm 0.84[3.6]$	$3.49 \pm 1.59[2.2]$	$-7.18 \pm 3.38[-2.1]$	$0.06 \pm 1.26[0.0]$

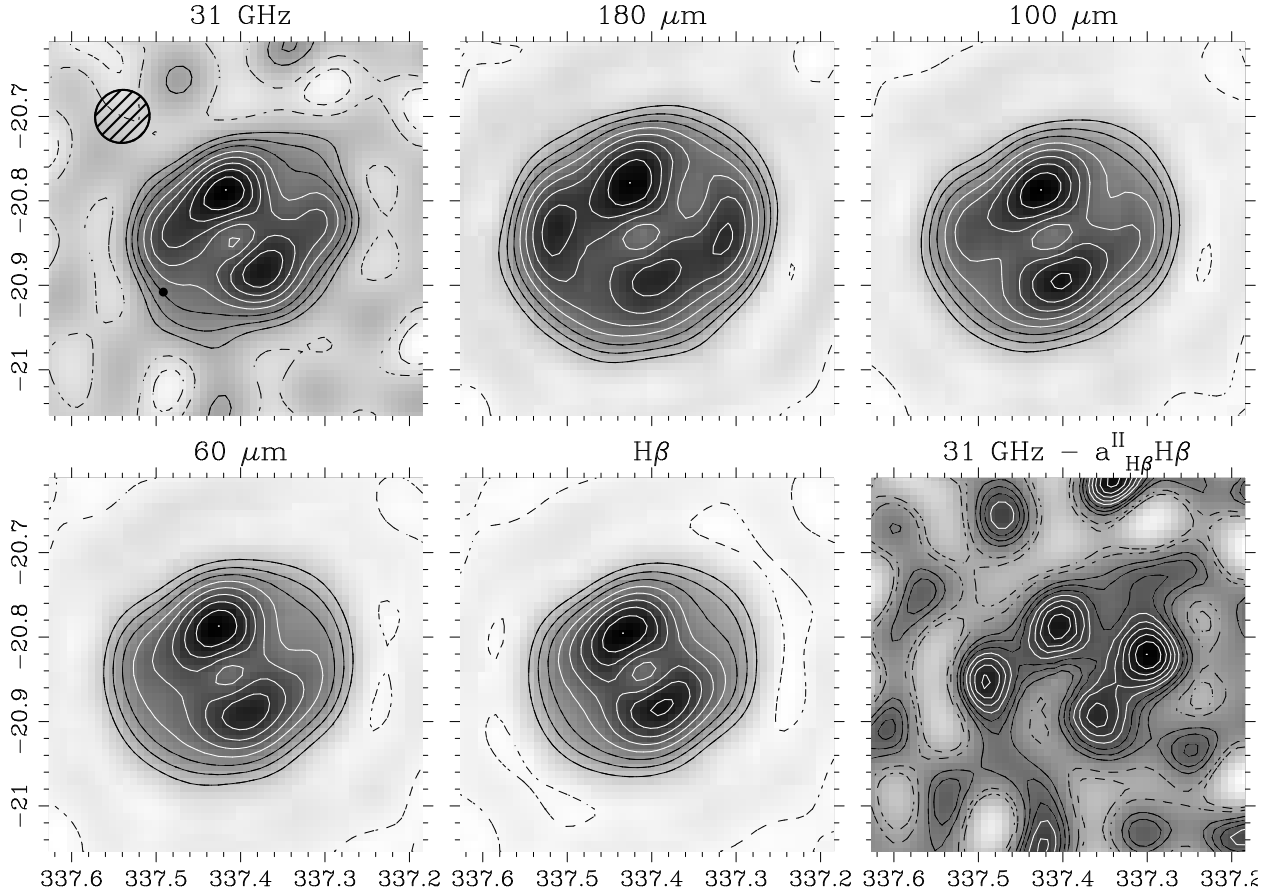


Fig. 2.— The Helix at 31 GHz, 100  $\mu\text{m}$ , 180  $\mu\text{m}$ , 60  $\mu\text{m}$ , and  $\text{H}\beta$ , as seen by the CBI: CBI observations have been simulated on the far-IR and  $\text{H}\beta$  image to enable a faithful comparison. The image on the lower right results after subtracting the appropriately scaled  $\text{H}\beta$  template from the CBI image (see Sec. 2.5), and shows the anomalous emission. Solid contour levels are linearly spaced in steps of 10% the maximum intensity, and start at 10%, and are overlaid for clarity on a linear gray scale image across the full range of intensity. Dotted contours are at the  $-10\%$  and zero levels. The beam ellipse shown on the 31 GHz image, with a size of  $3.89 \times 3.74 \text{ arcmin}^2$ , is the same for all images. The noise level and peak specific intensity are at 8.9 mJy/beam and 0.135 Jy/beam for the 31 GHz data. The black dot on the CBI image lies at the location of J2229-2054.

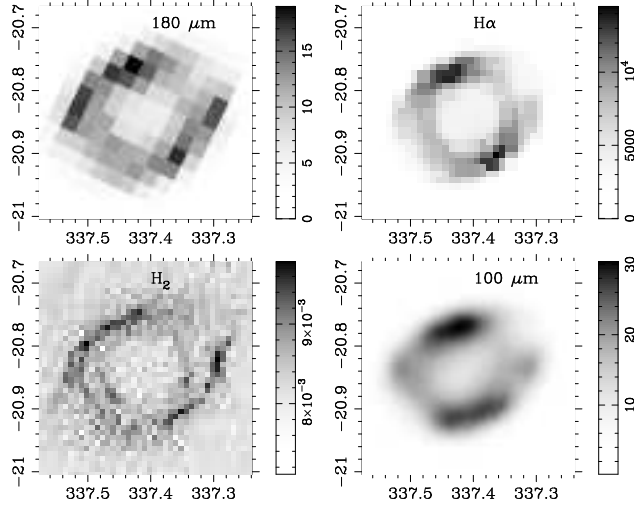


Fig. 3.— Comparison images at  $180 \mu\text{m}$ ,  $\text{H}\alpha$ ,  $\text{H}_2$  (after removing the two brightest stars in the field), and  $100 \mu\text{m}$ , highlighting the similarities between the far-IR images, and their differences with  $\text{H}\alpha$ .

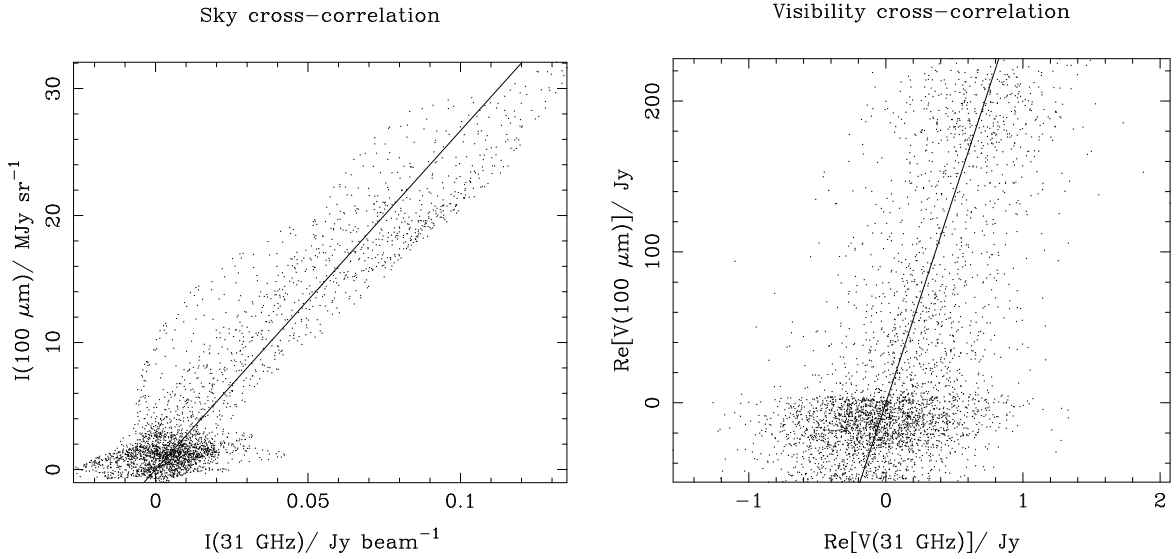


Fig. 4.— Sky plane (left) and frequency plane (right)  $100 \mu\text{m}$ – $31 \text{ GHz}$  correlations. The straight line fits have dimensionless slopes of  $3.45(2) \cdot 10^{-3}$  (sky) and  $3.61(7) \cdot 10^{-3}$  (visibilities).

to different angular scales, and different objects. We estimate the 12'-chopped observations from Finkbeiner et al. (2002) are sensitive to spatial frequencies ( $uv$ -range) in the range  $\sim 200\text{--}400 \text{ rad}^{-1}$ , similar to the CBI's (which roughly corresponds to angular scales of  $\sim 0.2 \text{ deg}$ ), while the data used by de Oliveira-Costa et al. (2002) are sensitive to multipoles lower than 30, roughly equivalent to angular scales of 12 deg.

The ratio  $a_{\text{H}\beta}^{\text{II}}/a_{\text{H}\beta}^{\text{I}} = 0.8$  can be used as an upper limit to the fractional level of free-free emission at 31 GHz: the single-component fit gives the conversion factor were all of the 31 GHz emission proportional to  $\text{H}\beta$ , while the two-component fit accounts for the presence of the  $100 \mu\text{m}$ -correlated component. This is an upper limit because there are indications (see Fig. 2 and the SED analysis in Sec. 4.2) that the  $100 \mu\text{m}$  image is not an ideal template for the anomalous emission at 31 GHz, so that part of it could be mistakenly attributed to  $\text{H}\beta$ .

Applying  $a_{\text{H}\beta}^{\text{II}}$  to the observed  $\text{H}\beta$  flux from O'Dell (1998) gives a 31 GHz free-free flux density of  $a_{\text{H}\beta}^{\text{II}} \times F(\text{H}\beta) = 2.12 \cdot 10^{+12} \times 3.37 \cdot 10^{-13} = 0.714 \text{ Jy}$ , or  $65 \pm 19\%$  of 1.096 Jy, our 31 GHz flux density for the Helix (assuming a 30% uncertainty on the  $\text{H}\beta$  measurement).

### 3. SIMBA observations

SIMBA, at SEST, is a 37-channel bolometer array, operating at 1.2 mm (250 GHz). The half-power beam-width of a single element is  $24''$ . We have observed the Helix on the 15 and 16 Aug. 2002, with a scanning speed of  $80'' \text{ s}^{-1}$ , and obtained 8 scans,  $1200'' \times 1000''$  each. The SIMBA scans are reduced in the standard manner using the MOPSI package written by Robert Zylka (IRAM, Grenoble). Flux calibration is carried out by comparison with Uranus maps.

The 250 GHz  $3\text{-}\sigma$  upper limit after sky noise filtering, destriping, and taking into account flux losses is 0.52 Jy, as we now explain. The  $3\text{-}\sigma$  limit without sky noise filtering (but with destriping) is 1.61 Jy.

#### 3.1. Flux loss estimates

SEST does not operate with a chopping secondary; as a substitute sky cancellation is obtained with channel-dependent bolometer filter functions, which cut out low spatial frequencies in SIMBA scans. The time sequence is multiplied by a complex bolometer filter function in frequency space (Reichert et al. 2001), leading to flux losses.

The  $1/2$  level, for frequencies below which the 37 channel filter functions have moduli lower than  $1/2$ , corresponds to an average and dispersion for all 37 filters of  $6.6 \pm 0.4 \cdot 10^{-2}$  Hz. With a scanning speed of  $80''/s$ , this is roughly equivalent to a low spatial frequency ‘hole’ in the  $uv$ -plane of radius  $170 \pm 10 \text{ rad}^{-1}$ . In order to estimate flux losses, we cut-out the simulated  $H\beta$  visibilities for the Helix with  $uv$ -radii under  $170 \text{ rad}^{-1}$ , and reconstruct with the maximum entropy algorithm in AIPS++ (the fitting of simple model components is no longer a good approximation when cutting  $uv$ -range). Aperture photometry of the whole nebula and comparison with the input template shows we recover 60% of the flux density.

### 3.2. Destriping and upper limit estimates on the 250 GHz flux densities

An important step in the reduction is a second sky cancellation, whose purpose is to minimize sky noise, performed by removing correlated signal among the 37 channels. This has been done with a search radius of  $100''$ , which in effect leaves only the outer ring of bolometer detectors for cross-correlation. In the case of the Helix part of the signal may have been removed - so we have also tried reducing without sky noise removal.

The SIMBA data are affected by scanning artifacts, which appear as noise stripes parallel to the mapping direction. We used a destriping algorithm in order to improve the noise of the SIMBA images. We worked on the Fourier amplitude image of each scan, where stripes stand out as straight lines crossing the origin (stripes have zero frequency in one direction, and are effectively 1D point sources in the orthogonal direction). Even faint stripes are very conspicuous in the Fourier amplitude image, and they are easily removed by median filtering as a function of radius, i.e. by stepping in distance from the frequency origin and median filtering all pixels in a given annular radial bin in the 2 D spatial frequency domain. We flag all visibilities whose moduli differ by more than  $3\sigma$  at a given  $uv$ -radius, and replace their value by an average of unflagged visibilities in other scans. Our destriping algorithm follows a standard technique, detailed examples of which can be found in Emerson & Gräve (1988), Davies et al. (1996), Schlegel et al. (1998), and its net effect is to reduce the noise by a factor of 2.2 in the case of sky-noise-filtered images, and a factor of 12.6 without sky-noise filtering. An example application of our destriping algorithm can be found in Hales et al. (2003).

The resulting  $1\sigma$  noise in the reduced SIMBA images is 25 mJy/beam with sky noise reduction, and 78 mJy/beam without, for a circular beam  $24''$  FWHM. In the Helix the bulk of optical emission is distributed in a ring, taking about  $1/3$  the solid angle of the whole nebula, and the peaks of emission are concentrated in clumps along the ring. We assume the bulk of emission, had it been detected, would have fallen on  $1/3$  of the solid angle subtended by a uniform disk,  $660''$  in diameter. This allows us to put  $3\sigma$  upper limits on the integrated

nebular flux density at 250 GHz of 0.52 Jy with sky noise reduction, and 1.61 Jy without, after correcting for 60% flux losses. The integrated flux density uncertainties were calculated by multiplying the noise per pixel in the final SIMBA image by  $\sqrt{N N_{\text{beam}}}$ , in a similar way as for the CBI photometry.

## 4. Comparison with other integrated flux measurements

### 4.1. Observed spectral energy distribution of the Helix

We have searched the literature for all existing measurements that allow setting up a SED for the Helix. A problem with the low-frequency data is background source contamination, which stands out in the 1.4 GHz image of Rodriguez et al. (2002). The 5 GHz data of Milne & Aller (1974) are distorted by a background source, as may be appreciated from Fig. 1 of Leene & Pottasch (1987), so we take their measurement of 1.292 Jy as an upper limit. Thus we also take the 2.7 GHz measurement of 1.27 Jy (Thomasson & Davies 1970) as an upper limit. On the other hand the measurement of  $0.68 \pm 0.2$  Jy at 0.408 GHz, from Calabretta (1982) and Calabretta (2003, private communication), and  $0.51 \pm 0.25$  Jy at 0.843 GHz, from Calabretta (1985), result after removal of background sources, and should be accurate estimates of the nebular emission. The *WMAP* first-year data release (Bennett et al. 2003) places upper limits on the Helix flux density, which we estimate at  $3\sigma$ , where  $\sigma$  is the rms point source sensitivity at the position of the Helix in 5 frequency bands. Fig. 6 summarizes the existing measurements, together with the results from this work.

The  $100\mu\text{m}$  and  $60\mu\text{m}$  *IRAS* bands, in contrast to the  $25\mu\text{m}$  and  $12\mu\text{m}$  bands, are reasonably free of line emission (Leene & Pottasch 1987; Speck et al. 2002), and should therefore trace dust. The ISOPHOT observations at  $180\mu\text{m}$ ,  $160\mu\text{m}$  and  $90\mu\text{m}$  in Speck et al. (2002, their Fig. 5) do not sample the whole nebula, but allow one to estimate the total flux densities at  $180\mu\text{m}$ ,  $160\mu\text{m}$  and  $90\mu\text{m}$  by approximately scaling to the  $100\mu\text{m}$  *IRAS* integrated flux density<sup>8</sup>.

---

<sup>8</sup>the  $90\mu\text{m}$  and  $180\mu\text{m}$  images of the whole Helix available from the *ISO* archive seem offset from zero, hinting at calibration problems, and would also require scaling

## 4.2. Problems with free-free emission

### 4.2.1. Extinction in the Helix

For free-free emission, radio continuum measurements can be used to predict optical recombination line fluxes, provided extinction is known. Extinction to the Helix is very low: the highest value of the  $H\beta$  extinction coefficient reported by Henry et al. (1999) is  $c = 0.13$ , for a slit position falling on the nebular ring. Such a small value for  $c$  is within the scatter for the Balmer decrement measured by Henry et al. (1999) in three slit positions. We assume extinction is negligible in the visible, as does O’Dell (1998).

### 4.2.2. Average electron temperature

Eq. A8 in Caplan & Deharveng (1986), also used in the PN NVSS survey of Condon & Kaplan (1998), allows one to predict an  $H\beta$  flux,  $F(H\beta)$  in  $10^{-15}$  W m $^{-2}$ , given a thermal radio continuum flux density  $F_\nu$  in mJy at frequency  $\nu$  in GHz and an electron temperature  $T_e$  in  $10^4$  K:

$$F(H\beta) = 0.28 T_e^{-0.52} \nu^{0.1} F_\nu. \quad (2)$$

Our flux-loss corrected 31 GHz flux density of 1096 mJy predicts  $F_c(H\beta) = 4.56 \cdot 10^{-13}$  W m $^{-2}$ , if the electron temperature is  $T_e = 9000$  K (O’Dell 1998; Henry et al. 1999), close but in excess of the  $H\beta$  flux reported by O’Dell (1998), of  $3.37 \cdot 10^{-13}$  W m $^{-2}$ . A value of  $T_e = 1.6 \pm 0.3 \cdot 10^4$  K is required to match the 31 GHz flux density to the  $H\beta$  flux. If  $T_e = 9000$  K, the expected level of free-free emission is 809 mJy, which is significantly less than the observed  $1096 \pm 100$  mJy.

But, as explained in Sec. 2.5, only part of the 31 GHz emission is proportional to  $H\beta$  (otherwise the 31 GHz and  $H\beta$  images would look the same). To match the upper limit free-free- $H\beta$  conversion factor obtained in Sec. 2.5,  $a_{H\beta}^{II} = (2.12 \pm 0.29) \cdot 10^{12}$  Jy /W m $^{-2}$ , the temperature must be brought down to  $7100 \pm 1900$  K. The required electron temperature for the 0.408 GHz data to match the  $H\beta$  flux, if dominated by optically thin free-free emission, is  $2800 \pm 1600$  K (assuming 30% uncertainties).

Surprisingly low values for the temperature of the photoionized gas in the Helix are obtained from two independent measurements (the 31 GHz- $H\beta$  conversion factor and the 0.408 GHz flux density), and their weighted average is  $T_e = 4600 \pm 1200$  K. This value is at odds with the electron temperature derived from collisionally excited lines (CELs), of  $\sim 9000$  K (O’Dell 1998; Henry et al. 1999). However, this discrepancy on  $T_e$  has previously been reported in H II regions and is an indication of temperature variations within the nebulae (Peimbert 1967). Our results are also reminiscent of the Balmer jump temperature and CEL

temperature discrepancy in other PNe, in particular in M 1-42 (Liu et al. 2001), where the BJ temperature is 3650 K, or  $\sim 5660$  K less than the CEL temperature. Other CEL-discrepant  $T_e$  diagnostics are the optical recombination line ratios, which also give very low values, e.g.  $< 2500$  K in Abell 30 (Wesson et al. 2003).

As a consistency check on Eq. 2 we compare the value of the  $H\beta$  recombination coefficient, fixed by matching the observed  $H\beta$  flux and the radio emission-measure, against the tables in Storey & Hummer (1995): we obtain  $9.47 \cdot 10^{-14} \text{ cm}^3\text{s}^{-1}$ , which matches case B of Baker & Menzel (1938) values of  $1.75 \cdot 10^{-13}$  at ( $T_e = 1000$  K,  $N_e = 100 \text{ cm}^{-3}$ ) and  $7.99 \cdot 10^{-14}$  at ( $T_e = 3000$  K,  $N_e = 100 \text{ cm}^{-3}$ ), or an interpolated temperature of 2688 K, and colder yet if case A of Baker & Menzel (1938) is assumed. We consider this value of the electron temperature is satisfactorily close to the 3000 K derived from Eq. A8 in Caplan & Deharveng (1986).

#### 4.2.3. *Electron temperature variations*

If there are temperature variations across the Helix then the free-free emission at 31 GHz is enhanced relative to  $H\beta$  in the hot gas. We use Eq. 2 to obtain the electron temperature map presented in Fig. 5, under the assumption that all of the 31 GHz emission is free-free.

The temperature structure cannot be explained in terms of photoionization, as models predict a drop in  $T_e$  with distance from the central star (Henry et al. 1999, their Fig. 8), while the temperature peaks on the nebular ring. Trying to explain the hot spots with shock excitation meets the difficulty that no fast wind has been detected in the Helix (Cerruti-Sola & Perinotto 1985; Cox et al. 1999).

Although their origin is undetermined, we cannot altogether discard that temperature fluctuations from 10 000 K to 40 000 K may account for the morphological differences between  $H\beta$  and 31 GHz. But this possibility seems rather contrived considering 1- the predicted temperatures are higher by 10 000 K than the [O III] diagnostic of  $9500 \pm 500$  K (Henry et al. 1999), and 2- only the Eastern lobe clearly stands out as a hot spot, while the other regions of anomalous emission maxima do not coincide with local  $T_e$  maxima.

#### 4.2.4. *SED modeling*

To emphasize the existence of anomalous radio emission in the Helix, we now try modeling the SED of the Helix only taking into account free-free and thermal vibrational emission from classical grains. We use simple radiative transfer in a cylindrical nebula, and the

`gffsub` routine in CLOUDY (Ferland 1996) for the free-free gaunt factor. Since we need to extrapolate free-free emissivities over a large range in frequency, we take care to validate the emissivity laws by comparison with Beckert (2000). We assume the abundances of singly and doubly ionized helium are as in Henry et al. (1999), and fix the nebular radius to 330 arcsec. The free parameters in our models are: The proton density  $N_p$ , the dust temperature  $T_d$ , dust flux density  $F_\nu$  at the reference frequency of 3000 GHz (or 100  $\mu\text{m}$ ), and the dust emissivity index  $\alpha$ , in the form  $F_\nu \propto \nu^\alpha B_\nu(T_d)$ . The optimization is carried-out with ‘Pikaia’, the genetic algorithm programmed by Charbonneau (1995).

The resulting SEDs are shown in Fig. 6: The dashed line fits the total CBI flux density with  $T_e = 10000$  K,  $T_d = 24$  K,  $\alpha = 2.43$ , while the solid line fits the measurement at 0.408 GHz (Calabretta 1982) with  $T_e = 3000$  K,  $T_d = 22$  K,  $\alpha = 2.8$ . Steep values of the dust emissivity index, of order 2.5, have indeed been reported for environments with  $T_d \sim 20$  K (Dupac et al. 2003). The best fit dust emissivity index and temperatures are constrained by the *WMAP* and SIMBA upper limit:  $\alpha = 0$  gives a best fit black body emission of  $\sim 1$  Jy at 31 GHz for grains at 36 K, and could otherwise account for the rise from 0.408 GHz to 31 GHz (see Fig. 6), and the 100  $\mu\text{m}$  correlation. An intermediate model, that would fit the far-infrared (far-IR) data and the CBI measurement with  $T_d = 24$  K and  $\alpha = 1$ , has a 250 GHz flux density of 60 Jy, and is ruled out by the SIMBA observations.

It is apparent from Fig. 6 that the 408 MHz and 31 GHz measurements cannot be reconciled under the free-free hypothesis. The level of free-free emission is a fraction of  $0.36 \pm 0.20$  at 31 GHz from this spectroscopic argument.

### 4.3. Ionized mass and filling factor

An emission measure of  $EM = 442.6 \text{ cm}^{-6} \text{ pc}$  is required to fit the 0.408 GHz flux density, and that part of the 31 GHz flux density that can be accounted for by free-free emission. Together with a uniform and cylindrical model nebula 330'' in radius at  $T_e = 3000$  K, this is a proton density of  $N_p = 26 \text{ cm}^{-3}$ , and an ionized mass of  $0.096 M_\odot$  (with a 30% accuracy that stems from the level of free-free emission at 31 GHz). If all of the 31 GHz flux density were due to bremsstrahlung and  $T_e = 10000$  K, then  $EM = 1721 \text{ cm}^{-6} \text{ pc}$  and  $N_e = 52 \text{ cm}^{-3}$ .

The Helix is so diluted that it is optically thin down to 100 MHz. For  $T_e = 10000$  K as well as for  $T_e = 3000$  K, the turnover frequency (at which the free-free optical depth is unity), is 30 MHz. Note that if the bulk of emission falls in 1/3 the solid angle subtended by a uniform disk,  $EM$  rises by a factor of 3, and the turnover frequency is then about 50 MHz.

However, the Helix is renowned for its cometary knot complex. The knots could have optically thick spectra: with a turn-over frequency of  $\nu_T \sim 1$  GHz, the knots would be optically thin and stand out at 31 GHz, and yet be optically thick and faint at 0.408 GHz. The difference between the 31 GHz flux of  $1096 \pm 100$  mJy and  $400 \pm 120$  mJy, the free-free continuum at 31 GHz extrapolated from the low-frequency data, or about  $f_{\text{knots}} = 63 \pm 11\%$  of the 31 GHz emission, would be due to the knots in their optically thin regime. The 31 GHz–100  $\mu\text{m}$  correlation would then follow by arguing most of the dust is in the knots. But in this model the difference between  $H\beta$  and 31 GHz (both optically thin) would stem from differential extinction of  $H\beta$  by the dust in the knots. Since the knots would not be seen in  $H\beta$  to account for the morphological differences with 31 GHz, the observed  $H\beta$  flux from the knots would vanish,  $F(H\beta^{\text{knots}})|_{\text{observed}} = 0$ , and the implied value of logarithmic  $H\beta$  extinction for the knot model would have to be

$$c = \log \left( \frac{(H\beta^{\text{diffuse}} + H\beta^{\text{knots}})|_{\text{dereddened}}}{H\beta^{\text{diffuse}}|_{\text{observed}}} \right) = -\log(1 - f_{\text{knots}}) = 0.43^{+0.15}_{-0.11}, \quad (3)$$

or  $A_V = 0.94$  with the extinction curve from Cardelli et al. (1989). Such an extinction coefficient would have been detected by (Henry et al. 1999) since their slit positions sample the nebular ring, which is rich in knots, but they report  $c < 0.13$ , a value which borders their measurement uncertainty on the Balmer decrement.

Even putting aside the extinction problem, a filling factor of  $\epsilon \sim 0.5$  from Henry et al. (1999) is far too high for the knot model. We investigated fitting the helix SED with two free-free components: An optically thin component and the optically thick knots, implemented as a core-halo model. The spectral behaviour of uniform clumps immersed in an optically thin and uniform slab is equivalent to that of an optically thick slab inset in a larger optically thin slab, as shown by Calabretta (1991). A turn-over frequency (at which the free-free opacity is unity) of 7 GHz is required to accommodate both the CBI and the 843 MHz spectral point. At  $T = 10000$  K,  $EM = 10^8 \text{ cm}^{-6}\text{pc}$  is required for  $\nu_T \sim 5$  GHz. When compared against the observed 31 GHz  $EM$ , this implies a filling factor  $\epsilon < 10^{-3}$ . Not only is this value three orders of magnitude lower than measured, but it is also very unusual for the ionized gas in PNe (although common for the molecular component).

The density reported by Henry et al. (1999) varies between  $30 \text{ cm}^{-3}$  and upper limits of  $100 \text{ cm}^{-3}$ , so the filling factor implied by the radio data is also  $\sim 0.5 - 1$ . For the core-halo model to account for the observed SED, the density in the clumps would have to be of order  $> 10^3 \text{ cm}^{-3}$ , assuming the turn-over frequency of the core is above 4 GHz and for the halo below 0.408 GHz, and using the ratio of optically thin flux densities of both components (Mark Calabretta, private communication). That the density diagnostics used by Henry et al. (1999) miss the high density gas because of extinction in the clumps meets the difficulty

that no significant extinction is measured with the Balmer decrement. By comparison to other PNe, the optical spectra of the Helix resolve very fine details relative to the bulk nebular properties obtained from the integrated measurements. Thus the filling factor of the Helix would be one of the best determined, if it wasn't for the uncertainties inherent to low-density measurements, which can only take it closer to 1.

Given the central role of the filling factor for the interpretation of the helix SED, we searched the literature for PNe with very low value of  $\epsilon$ . The only study that has reached values of order  $\epsilon \sim 10^{-3}$  for the Helix is Boffi & Stanghellini (1994), with  $\epsilon = 5 \cdot 10^{-3}$ . But we doubt the validity of this value, as we now explain. The statistical analysis of Boffi & Stanghellini (1994) is based on pre-1978 data compiled by Stanghellini & Kaler (1989), in which the density-diagnostic line ratios used for the Helix are at the low-density limit of their validity. In Stanghellini & Kaler (1989) the derived electron density of the Helix is an upper limit only, of  $N_e < 200 \text{ cm}^{-3}$  (with substantial scatter). Moreover, Boffi & Stanghellini (1994) do not quote the right value from Stanghellini & Kaler (1989) (2.8 against 2.3 for  $\log N_e$ ), and their  $H\beta$  flux is too high by 50% when compared with O'Dell (1998).

#### 4.4. Candidate emission mechanisms at 31 GHz

##### 4.4.1. *The unsuitability of synchrotron or very cold grains*

What is responsible for the 31 GHz excess? Synchrotron emission is not a suitable candidate because free-free opacity cannot account for the turnover at  $\sim 1\text{--}20$  GHz, while synchrotron opacity is not expected to be significant in a faint object, 10 arcmin in size. Moreover synchrotron emission has never been convincingly reported in a PN<sup>9</sup>, while evidence for magnetic fields is only available in very young proto-PNe (Miranda et al. 2001). The record size of the Helix precludes the survival of a significant magnetic field, which in a magnetized wind decreases as the inverse distance of the central star.

The 250 GHz and *WMAP* upper limits constrain the dust emissivity index to a value steep enough to rule out any vibrational dust emission below 100 GHz, for a standard grain population. But could there be ultra-cold grains in the Helix, accounting for half the 31 GHz emission, or  $\sim 0.5$  Jy, and simultaneously reach levels of  $\sim 2$  Jy at 250 GHz, thereby reconciling the SEST and CBI measurements? The emissivity index for such grains would have to be close to zero, to give them a broad spectrum, and their temperature less than 3 K. Fig. 6 shows an example black-body at 3 K. Temperatures lower than 3 K have indeed

---

<sup>9</sup>the data mentioned by Dgani & Soker (1998) remains unpublished

been observed in the Boomerang nebula (a post-AGB object undergoing heavy mass-loss) through CO(1–0) absorption against the CMB (Sahai & Nyman 1997). The hot (i.e. 20 K) and cold (i.e. 3 K) dust components have different emissivities: The requirement  $\alpha = 0$  at  $\nu = 300$  GHz implies grain sizes of order the wavelength of  $\sim 1$  mm, while we fit the far-IR data with  $\alpha = 2$ . For grains of a single size  $a$ , with mass density of  $\rho = 1 \text{ g cm}^{-3}$ ,

$$M_{\text{dust}} = \frac{4}{3} \rho \frac{a}{Q_a(\nu)} D^2 \frac{F_\nu}{B_\nu}, \quad (4)$$

assuming optically thin grains, and where  $F_\nu$  is the observed flux density and  $B_\nu$  is the Planck function. With the absorption cross sections from Laor & Draine (1993)<sup>10</sup>, we have  $M_{\text{cold}}^{\text{dust}} = 1.1 M_\odot$  for 10  $\mu\text{m}$ -sized silicate grains (the largest size for which data are available), and  $M_{\text{hot}}^{\text{dust}} = 5.5 \cdot 10^{-3} M_\odot$  for 0.1  $\mu\text{m}$ -sized grains. The implied cold dust opacity at 300 GHz is  $\chi_\nu = 1.04 \text{ cm}^2 \text{g}^{-1}$ , in agreement with the value adopted by Jura et al. (2001) for mixed-size grains with  $\alpha = 0$ , and with the observed value of  $\chi_\nu = 0.35 \text{ cm}^2 \text{g}^{-1}$  in Barnard 68 (Bianchi et al. 2003). Thus the hypothetical cold component would account for most of the total molecular mass. Although no CO(1–0) data are available in the literature to test for absorption, we can also discard this cold component on the grounds that its obvious location would be the cometary knots, but their CO temperature is  $\sim 18$ –40 K (Huggins et al. 2002).

Lagache (2003) suggests that VSGs (such as PAHs or ultra-small silicates) could reach very low temperatures after radiative de-excitation. At 3 K the very cold VSGs would have a SED with a significant Rayleigh-Jeans tail at 30 GHz. But we performed the same analysis as for the very large grains and obtained that the cold dust mass would have to be even higher than for the large grains: Using the absorption cross sections  $Q_a$  from Laor & Draine (1993) for the smallest PAHs and the largest silicate grains,

$$a/Q_a(\nu)|_{a=3.5 \cdot 10^{-4} \mu\text{m}} = 22.6 a/Q_a(\nu)|_{a=10^7 \mu\text{m}}. \quad (5)$$

#### 4.4.2. *New dust emission mechanisms at 31 GHz*

This leaves only two other candidates for the observed 31 GHz excess: electric dipole emission from spinning very small dust grains (Draine & Lazarian 1998, spinning dust), or magnetic dipole emission from classical grains (Draine & Lazarian 1999).

VSGs are essential for the spinning dust mechanism: equipartition of rotational energy ensures only the smallest grains,  $\sim 100$  atoms in size, will rotate at 31 GHz. But the evolutionary trend in PNe is toward a decreasing fraction of mid-IR luminosity with size, in the

---

<sup>10</sup>extracted from [www.astro.princeton.edu/~draine/](http://www.astro.princeton.edu/~draine/)

sense that mid-IR-bright PNe are the most compact, and hence the youngest (Pottash et al. 1984). If VSGs always emit at mid-IR wavelengths, then they are not expected to be present in PNe as evolved as the Helix. Leene & Pottasch (1987) have shown that the 12  $\mu\text{m}$ -band IRAS flux from the Helix can be entirely accounted for by emission lines, suggesting little mid-IR continuum.

The report on ISOCAM observations of the Helix (Cox et al. 1999) highlights the absence of VSGs in the Helix, through the absence of characteristic PAH features and of detectable continuum at mid-IR wavelengths. However, this claim is unfounded because the ISOCAM CVF pointings sample the outskirts of the nebula<sup>11</sup>, and cannot be extrapolated to the whole of the Helix. Furthermore, the ISOCAM CVF spectrum lacks the sensitivity to place useful limits on the level of the mid-IR continuum: a noise of  $\sim 1 \text{ MJy sr}^{-1}$  is visible in Fig. 1 of Cox et al. (1999), which when extrapolated to the whole of the Helix is a  $3 \sigma$  limit on the total flux density of 20 Jy, while the IRAS 12  $\mu\text{m}$  flux density is 11 Jy.

#### 4.4.3. 26–36 GHz to 100 $\mu\text{m}$ conversion factors, and their spectral index

By itself the spectrum of the Helix in the 10 CBI channels is too noisy to place useful constraints on the spectral index. But assuming the 100  $\mu\text{m}$  HIRES map is a good template of the 31 GHz emission, we can use the frequency dependence of the 100 $\mu\text{m}$ –31 GHz conversion factors, which are determined with good accuracy, to obtain a 26–36 GHz SED for the Helix.

The determination of the 26–36 GHz spectral index derived with the use of a template has better fractional accuracy than without. The improved accuracy stems from assuming the morphology of the Helix is known (fixed to that of 100  $\mu\text{m}$ ), so that only the 31 GHz–100  $\mu\text{m}$  conversion factor is kept as a free-parameter. But of course it must be kept in mind the 31 GHz and 100  $\mu\text{m}$  maps are not strictly identical. We provide this SED to help modeling efforts aimed at studying the new dust emission mechanism, and as a comparison point with Finkbeiner et al. (2002). However, we caution the two-component fit with the  $\text{H}\beta$  and 100  $\mu\text{m}$  templates is more significant than the conversion factors used here, although the  $a^I$  coefficients are too noisy to set-up a SED.

We obtained frequency-dependent conversion factors by cross-correlating the real parts of the visibilities in each of the 10 CBI channels with the 100 $\mu\text{m}$  HIRES map (after simulating the CBI  $uv$ -coverage). The spectrum for the 31 GHz emissivity per nucleon, shown in Fig. 7, results after multiplying the frequency-dependent  $a^I(100 \mu\text{m})$  with the peak specific intensity

---

<sup>11</sup>namely the western rim visible in  $\text{H}_2$  emission-line images

at 100  $\mu\text{m}$  (22.9 MJy/sr in the CBI-simulated map), and dividing with an estimate of the peak nucleon column density:  $j_\nu/n_{\text{H}} = I(31 \text{ GHz})/N_{\text{H}}$ , with  $N_{\text{H}} = 3.94 \cdot 10^{20} \text{ cm}^{-2}$  for  $n_{\text{H}} = 200 \text{ cm}^{-3}$  and a depth of 0.64 pc (approximately the diameter of the Helix). In the Helix the molecular mass is  $0.025 M_{\odot}$  (Young et al. 1999), and the atomic mass is  $0.07 M_{\odot}$  (Rodriguez et al. 2002), which together represent about as much as the ionized mass of  $0.096 M_{\odot}$  (this work). Thus our estimate for the average nucleon density along the line of sight of peak 31 GHz specific intensity assumes about half the total mass is ionized, for which the peak electron density is about  $100 \text{ cm}^{-3}$ .

The dashed lines in Fig. 7 are power-law fits to the data, with  $\alpha = -0.216_{-0.62}^{+0.67}$ , which is more accurate than the photometry of Section 2.1, but still too noisy to discriminate candidate emission mechanisms. The emissivity values in the Helix, from Fig. 7, are a factor of 2–3 higher than the 31 GHz emissivities in LPH 201.6, from Fig. 5 in Finkbeiner et al. (2002). But we draw attention to the fact that Finkbeiner et al. (2002) used an extinction-based nucleon density estimate, which is useless in the Helix because of its anomalously high gas to dust ratio of 1000 (Speck et al. 2002). Considering the uncertainties involved in the comparison, it appears  $j_\nu/n_{\text{H}}$  in the Helix and LPH 201.6 are of the same order.

Another interesting similarity with LPH 201.6 is that the feature which cannot be explained by free-free emission is a 5–10 GHz rise in flux density, as it would require unrealistic emission measures for a diffuse H II region. This is also one of the problems with free-free emission in the Helix (see Sec. 4.2).

#### 4.4.4. *Can the 31 GHz excess be explained in terms of predicted magnetic dipole emissivities?*

Draine & Lazarian (1999) caution that magnetic dipole emission could significantly contribute to the diffuse anomalous foreground if ferromagnetic grains are abundant. Iron is strongly depleted in dust grains in most PNe (Shields 1983; Oliva et al. 1996), this is perhaps also the case in the Helix. An ionization-bounded CLOUDY model based on the line fluxes and analysis from Henry et al. (1999) that reproduces [N II]  $\lambda\lambda 6548, 6584$  as well as [S II]  $\lambda\lambda 6716, 6731$  (with a sulfur depletion<sup>12</sup> of [S/H] =  $-1$ ), predicts that  $F([\text{Fe II}] \lambda 4300) = 3.5 \cdot 10^{-2} F(\text{H}\beta)$ . But [Fe II]  $\lambda 4300$  is absent from the spectrum reported by Henry et al. (1999), while nearby He II  $\lambda 4026$  is detected, with a flux of  $2.8 \cdot 10^{-3} F(\text{H}\beta)$ . If He II  $\lambda 4026$  is at the limit of detection, the implied iron depletion is [Fe/H] <  $-1$ , or less than a tenth solar.

---

<sup>12</sup>the difference between nebular and solar logarithmic abundance

The emissivities shown in Fig. 7 are a factor 10–20 too large to be interpreted in terms of the spinning dust or magnetic dipole emissivities calculated by Draine & Lazarian (1998, 1999). However, part of the 31GHz emission is indeed free-free, so that a 31 GHz emissivity per nucleon derived from the 31 GHz excess is better suited to test the model predictions. We have estimated this excess to represent at least 20% of the 31 GHz emission. This lower limit derives from the linear combination fits to the 31 GHz visibilities using the 100  $\mu\text{m}$  and  $\text{H}\beta$  templates. Applying  $a^{II}(100 \mu\text{m})$  to the peak 100  $\mu\text{m}$  intensity, and using a peak nucleon column density as above, of  $N_{\text{H}} = 3.94 \cdot 10^{20} \text{ cm}^{-2}$ , we obtain  $j_{\nu}/n_{\text{H}} = (4.3 \pm 2.3) \cdot 10^{-17} \text{ Jy sr}^{-1} \text{ cm}^2$ , now in closer agreement with the highest magnetic dipole emissivity from Draine & Lazarian (1999), of  $8 \cdot 10^{-18} \text{ Jy sr}^{-1} \text{ cm}^2$  at 31 GHz, but still a factor of 5 too large.

The factor of 5 difference between the theoretical magnetic dipole emissivities of the anomalous component could be due to different grain temperatures: Dust grains at  $T_d = 100 \text{ K}$  are usual in PNe, while the “cold neutral medium” environment used by Draine & Lazarian (1999) is set at  $T_d = 18 \text{ K}$ , and the grain emissivities scale linearly with  $T_d$  in the Rayleigh-Jeans approximation. The part of the grain population that is ferromagnetic could be confined to the ionized phase, where there is evidence for Fe depletion. This would explain why the anomalous emission map is more compact than the 180  $\mu\text{m}$  map. But the magnetic dipole emissivities are difficult to tailor to the Helix because the relative number densities of ferromagnetic grains  $n_{\text{gr}}/n_{\text{H}}$  is underdetermined: a small population of very hot grains could also account for the observations.

## 5. Conclusions

The CBI maps and the SIMBA flux density upper limit, which represent the highest frequency radio observations of the Helix to date, have allowed us to investigate the nature of radio-emission mechanisms in a diffuse circum-stellar environment. We reach the following results:

1. The 31 GHz map of the Helix follows a linear combination of the 100 $\mu\text{m}$  and  $\text{H}\beta$  images.
2. The fractional level of free-free emission at 31 GHz ranges from  $f = 36\%$  to  $f = 80\%$  from three arguments: 1- A morphological argument, from the ratio of  $\text{H}\beta$  coefficients in the single- and two-component linear combination fits, which gives an upper limit  $f = 80 \pm 16\%$ , 2- the same morphological argument coupled with the observed  $\text{H}\beta$  flux, which gives  $f = 65 \pm 19\%$  and 3- a spectroscopic argument, by comparison with

low-frequency measurements, which gives a lower limit  $f = 36 \pm 20\%$ .  $f = 100\%$  is inconsistent with the 250 GHz upper limit flux density (with sky-noise reduction).

3. A consequence of the reduced level of free-free emission in the Helix is a revision of the electronic temperature for the free-free emitting gas to  $T_e = 4600 \pm 1200$  K.
4. Differential extinction cannot account for the 31 GHz excess and morphological differences with  $H\beta$  because a value of  $A_V = 0.94$  mag would be required, while negligible extinction values of  $A_V < 0.28$  mag have been reported elsewhere from optical spectra.
5. The dust-correlated 31 GHz excess over free-free emission cannot be explained in terms of a synchrotron component, nor with optically thick knots, nor in terms of ultra-cold grains of any size (as constrained by the 250 GHz flux density upper limit).
6. We construct a map of the anomalous 31 GHz emission by subtracting the  $H\beta$  template image to the expected level of free-free emission. This map is similar to the far-IR templates, but is more compact, and has a much brighter Western lobe (or Western rim) relative to the rest of the nebula, a feature which is only seen in  $H_2$  emission line images of the Helix.
7. Of the two models proposed by Draine & Lazarian (1998, 1999) to account for the anomalous foreground, we favor magnetic dipole emission from ferromagnetic grains over spinning dust, because of the strong iron depletion onto dust grains and of the suspected lack of VSGs in the Helix. The inferred emissivity per nucleon for the 31 GHz excess is within a factor of five of the most optimistic magnetic dipole emissivities for the “cold neutral medium”, which can be explained in terms of a dust temperature five times hotter than  $T_d = 18$  K.
8. The 31 GHz– $100\mu\text{m}$  conversion factor in the Helix is similar to the value obtained by Finkbeiner et al. (2002) in the diffuse H II region LPH 201.6. This agreement suggests the same dust emission mechanism is responsible for the 31 GHz excess in both objects.

We are very grateful to the following: an anonymous referee for very interesting comments which improved the paper and also motivated Sec. 4.4.3 and Sec. 4.4.4; Mike Barlow for interesting suggestions, for pointing out the role of the cometary knot complex, and for corrections to the manuscript; Mark Calabretta for additional information on his low-frequency measurements and interesting comments on the free-free SED; Luis Felipe Rodriguez for providing the 1.4 GHz image; Angela Speck for providing useful comparison images; Tom Wilson for a critical reading. This work made use of the Southern H-Alpha Sky Survey Atlas

(SHASSA), which is supported by the National Science Foundation. S.C. acknowledges support from FONDECYT grant 3010037. S.C. and L.B. acknowledge support from the Chilean Center for Astrophysics FONDAP 15010003. We gratefully acknowledge the generous support of Maxine and Ronald Linde, Cecil and Sally Drinkward, Barbara and Stanely Rawn, Jr., and Fred Kavli. This work is supported by the National Science Foundation under grant AST 00-98734.

## REFERENCES

- Beckert, T., Duschl, W.J., Mezger, P.G., 2000, *A&A*, 356, 1149
- Baker, J.G, Menzel, D.H., 1938, *ApJ*, 88, 52
- Bennett, C. L., Halpern, M., Hinshaw, G., Jarosik, N., Kogut, A. , Limon, M., Meyer, S. S., Page, L., Spergel, D. N., Tucker, G. S., Wollack, E., Wright, E. L., Barnes, C., Greason, M. R., Hill, R. S., Komatsu, E., Nolta, M. R. , Odegard, N., Peirs, H. V. , Verde, L., Weiland, J. L., 2003, *ApJ*, *in press*, astro-ph/0302207
- Boffi, F.R., Stanghellini, L., 1994, *A&A*, 284, 248
- Bianchi, S., Gonçalves, J., Albrecht, M., Caselli, P., Chini, R., Galli, D., Walmsley, M., 2003, *A&A*, 399, L43
- Calabretta, M.R., 1982, *MNRAS*, 199, 141
- Calabretta, M.R., 1985, Ph.D. thesis, "A Radio Study of Southern Planetary Nebulae", University of Sydney, School of Physics (Dept. of Astrophysics)
- Calabretta, M.R., 1991, *Aust. J. Phys.*, 44, 441-58.
- Caplan, J., Deharveng, L., 1986, *A&A*, 155, 297
- Cardelli, J.A., Clayton, G.C., Mathis, J.S., 1989, *ApJ*, 345, 245
- Cerutti-Sola, M., Perinotto, M., 1985, *ApJ*, 291, 237
- Charbonneau, P., 1995, *ApJS*, 101, 309
- Condon, J.J., Broderick, J.J., Seielstad, G.A., 1991, *AJ* 102, 2041
- Condon, J.J., Cotton, W.D., Greisen, E.W., Yin, Q.F., Perley, R.A., Taylor, G.B., Broderick, J.J., 1998, *AJ*, 115, 1693

- Condon, J.J, Kaplan, D.L., 1998, ApJS, 117, 361
- Cox, P., Boulanger, F., Huggins, P. J., Tielens, A. G. G. M., Forveille, T., Bachiller, R., Cesarsky, D., Jones, A. P., Young, K., Roelfsema, P. R., Cernicharo, J., 1998, ApJ, 495, L23
- Davies, R.D., Watson, R.A., Gutiérrez, C.M, 1996, MNRAS, 278, 925
- Dgani, R., Soker, N., 1998, ApJ, 499, L83
- de Oliveira-Costa, A, Tegmark, M., Finkbeiner, D.P., Davies, R.D., Gutierrez, C.M., Haffner, L.M., Jones, A.W., Lasenby, A.N., Rebolo, R., Reynolds, R.J., Tufte, S.L., Watson, R.A., 2002, ApJ, 567, 363
- de Oliveira-Costa, A., Tegmark, M., Gutierrez, C.M., Jones, A.W., Davies, R.D., Lasenby, A.N., Rebolo, R., Watson, R.A., 1999, ApJ, 527, 9
- Draine, B.T., Lazarian, A., 1998, ApJ, 494, L19
- Draine, B.T., Lazarian, A., 1998, ApJ, 508, 157
- Draine, B.T., Lazarian, A., 1999, ApJ, 512, 740
- Dupac, X., Bernard, J.-P., Boudet, N., Giard, M., Lamarre, J.-M., Mény, C., Pajot, F., Ristorcelli, I., 2003, proceeding “Multi-Wavelength Cosmology” conference held in Mykonos, Greece, June 2003, ed. Kluwer, *in press*
- Emerson, D.T., Gräve, R., 1988, A&A 190, 353
- Ferland G.J., 1996, *Hazy, a brief introduction to Cloudy*, University of Kentucky Department of Physics and Astronomy Internal Report (Hazy)
- Finkbeiner, D.P., Schlegel, D.J., Frank, C., Heiles, C., 2002, ApJ, 566, 898
- Gaustad, J.E., McCullough, P.R., Rosing, W., Van Buren, D., 2001, PASP, 113, 1326
- Hales, A., Casassus, S., Alvarez, H., May, J., Bronfman, L., Readhead, A.C., Pearson, T.J., Mason, B.S., Dodson, R., 2003, ApJ, *in preparation*
- Harris, H.C, Dahn, C.C., Monet, D.G., Pier, J.R., 1997, IAU symp. 180, Planetary Nebulae, ed. H.J. Habing, H.J.G.L. Lamers (Dordrecht: Kluwer), 40
- Henry, R.B.C., Kwitter, K.B., Dufour, R.J., 1999, ApJ, 517, 782

- Huggins, P.J., Forveille, T., Bachiller, R., Cox, P., Ageorges, N., Walsh, J.R., 2002, ApJ, 573, L55.
- Jura, M., Webb, R.A., Kahane, C., 2001, ApJ, 550, L71
- Kogut, A., Banday, A.J., Bennett, C.L., Gorski, K.M., Hinshaw, G., Reach, W.T., 1996, ApJ, 460, 1
- Laor, A, Draine, B.T., 1993, ApJ, 402,441
- Lagache, G.,2003, A&A, *in press*
- Lang,K.R., 1980, “Astrophysical Formulae”, Springer-Verlag
- Leene, A., Pottasch, S.R., 1987, A&A, 173, 145
- Leitch, E.M., Readhead, A.C.S., Pearson, T.J., Myers, S.T., ApJ486, L23
- Lemke, D. et al 1996, A&A315, L64
- Liu, X.-W., Luo, S.-G., Barlow, M. J., Danziger, I. J., Storey, P. J., 2001, MNRAS, 327, 141
- Mason, B. S. , Pearson, T. J., Readhead, A. C. S. , Shepherd, M.C. Sievers, J. L., Udomprasert, P. S., Cartwright, J. K., Farmer, A. J., Padin, S., Myers, S. T., Bond, J. R., Contaldi, C. R., Pen, U.-L., Prunet, S., Pogosyan, D., Carlstrom, J. E., Kovac, J., Leitch, E. M., Pryke, C., Halverson, N. W., Holzappel, W. L., Altamirano, P., Bronfman, L., Casassus, S., May, J., Joy, M., 2003, ApJ, 591, 540
- McCullough P.R., Chen, R.R., 2002, ApJ, 566, 45
- Milne D.K., Aller, L.H., 1974, Galactic Radio Astronomy, eds. F.J.Kerr, S.C., Simonson, p. 411
- Milne, D.K., Aller, L.H., 1982, A&AS, 50, 209
- Miranda, L.F., Gomez, Y., Anglada, G., Torrelles, J.M., 2001, Nature, 414, 284
- Nyman, L.Å., Lerner, E.A., Nielbock, M., et al., 2001, The Messenger (ESO), 106, 40
- O’Dell, C.B., 1998, AJ, 116, 1346
- Oliva, E., Salvatti, M., Moorwood, A.F.M., Marconi, A., 1994, A&A, 288, 457
- Osterbrock D.E., 1989, “Astrophysics of Gaseous Nebulae and Active Galactic Nuclei”, W.H.Freeman and Company, San Francisco

- Padin, S., et al, 2002, PASP, 114, 83
- Page, L., Barnes, C., Hinshaw, G., Spergel, D. N., Weiland, J. L., Wollack, E., Bennett, C. L., Halpern, M., Jarosik, N., Kogut, A., Limon, M., Meyer, S. S., Tucker, G. S., Wright, E. L., 2003, ApJS, 148, 39
- Peimbert, M., 1967, ApJ, 150, 825
- Pottasch, S.R., Baud, B., Beintema, D., Emerson, J., Harris, S., Habing, H.J., Houck, J., Jennings, R., Marsden, P., 1984, A&A, 138, 10
- Readhead, A.C.R, Pearson, T.J., 2003, in Carnegie Observatories Astrophysics Series, Vol. 2: Measuring and Modeling the Universe, ed. W. L. Freedman (Cambridge: Cambridge Univ. Press);
- Reichert, L. A., Weferling, B., Esch, W., Kreysa, E., 2001, A&A, 379, 735
- Rodriguez, L.F., Goss, W.M., Williams, R., 2002, ApJ, 574, 179
- Sahai, R., Nyman, L-Å, ApJ, 487, L155
- Schlegel, D.J., Finkbeiner, D.P., Davis, M., 1998, ApJ 500, 525
- Shepherd, M.C., 1997, in Astronomical Data Analysis Software and Systems VI, ed. G Hunt & H.E. Payne, ASP conference series, v125, 77-84 “Difmap: an interactive program for synthesis imaging”.
- Shields, G.A., 1983, in Flower D.R., ed., IAU Symp. 103, Planetary Nebulae, Kluwer, Dordrecht, p. 259
- Speck, A.K., Meixner, M., Fond, D., McCullough, P.R., Moser, D.E., Ueta, T., 2003, AJ, 123, 346
- Stanghellini, L., Kaler, J.B., 1989, ApJ, 343, 811
- Storey, P.J., Hummer, D.G., 1995, MNRAS, 272, 41
- Thomasson, P., Davies, J.G, 1970, MNRAS, 150, 359
- Wesson, R., Liu, X.-W., Barlow, M. J., 2003, MNRAS, 340, 253
- Young, K., Cox, P., Huggins, P.J., Forveille, T., Bachiller, R., 1999, ApJ, 522, 387
- Zijlstra, A.A., Pottasch, S.R., Bignelli, C., 1989, A&AS, 79, 329



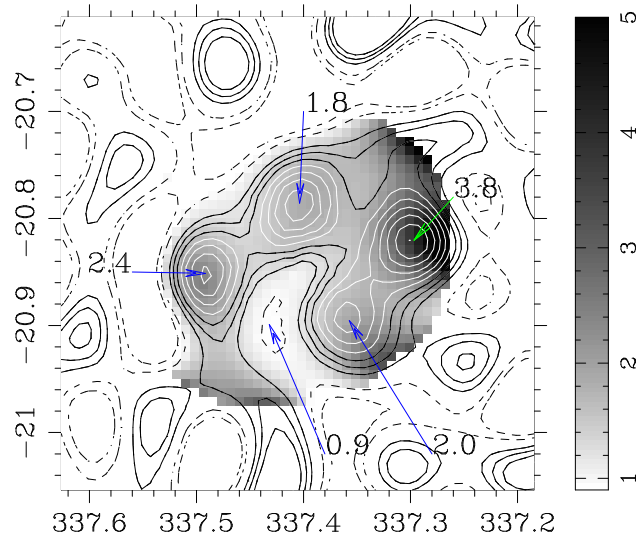


Fig. 5.— Electron temperature map in gray scale, with an overlay of the anomalous 31 GHz emission from Fig. 2 in contours. Units are  $10^4$  K, and the value of  $T_e$  are indicated at four selected positions.

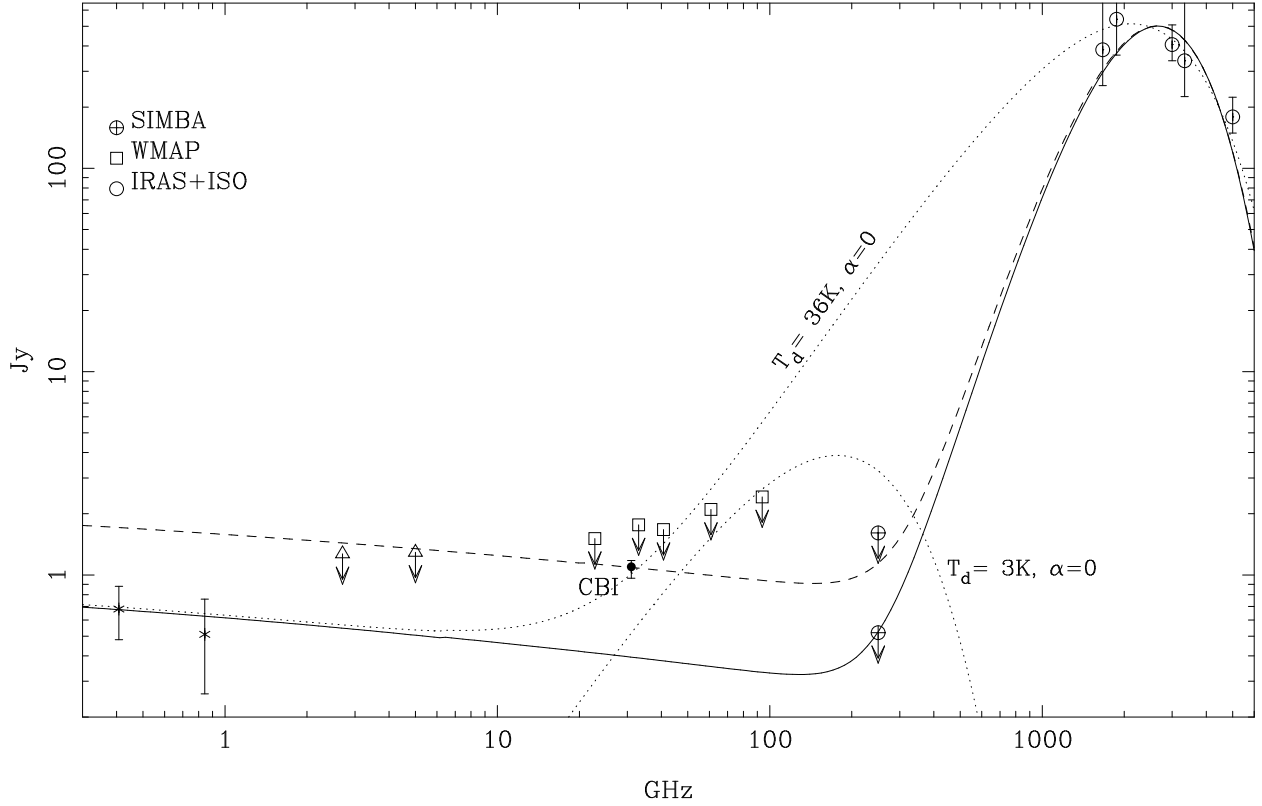


Fig. 6.— Spectral energy distribution of the Helix. The solid line is a theoretical SED composed of thermal vibrational dust and free-free emission, where the latter uses the CLOUDY Gaunt factor and is designed to fit the measurement at 408 MHz (Calabretta 1982) and the *IRAS* and ISOPHOT data (with 20% and 50% errors, respectively). The dashed line is a model designed to fit the CBI total flux density, drawn to emphasize the disagreement with low frequency observations. All arrows denote upper limits, and the two SIMBA points correspond to the limits with (lower) and without (higher) sky-noise reduction. The dotted lines show two black-body curves used to rule-out large grain emission as responsible for the 31 GHz excess. See text for information on the other measurements.

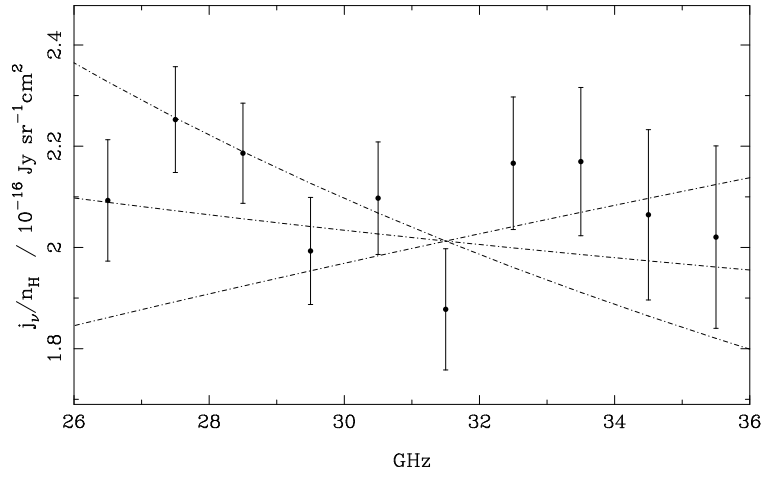


Fig. 7.— The 26–36 GHz emissivity per nucleon, calculated by multiplying the peak specific intensity at  $100 \mu\text{m}$  ( $22.9 \text{ MJy/sr}$  in the CBI-simulated map) with the frequency-dependent conversion factors  $a^I(100 \mu\text{m})$ . The dashed lines are power-law fits to the data (see text).